
Article:
Fatehifar, M., Revell, A., Jabbari, M. et al. (2023) A numerical analysis of particle encapsulation in a flow-focusing droplet generation device. Physics of Fluids, 35 (11). 113317. ISSN: 1070-6631

https://doi.org/10.1063/5.0172483

Physics of Fluids

RESEARCH ARTICLE | NOVEMBER 16 2023

A numerical analysis of particle encapsulation in a flow-focusing droplet generation device

Maryam Fatehifar ; Alistair Revell ; Masoud Jabbari ; Alessandro De Rosis

Physics of Fluids 35, 113317 (2023)
https://doi.org/10.1063/5.0172483

Physics of Fluids ARTICLE pubs.aip.org/aip/pof

A numerical analysis of particle encapsulation in a flow-focusing droplet generation device

Cite as: Phys. Fluids **35**, 113317 (2023); doi: 10.1063/5.0172483
Submitted: 16 August 2023 · Accepted: 23 October 2023 ·
Published Online: 16 November 2023

Maryam Fatehifar,[1,a)] Alistair Revell,[1] Masoud Jabbari,[2] and Alessandro De Rosis[1]

AFFILIATIONS

[1]Department of Fluids and Environment, School of Engineering, The University of Manchester, Manchester M13 9PL, United Kingdom
[2]School of Mechanical Engineering, University of Leeds, Leeds LS2 9JT, United Kingdom

[a)]**Author to whom correspondence should be addressed:** maryam.fatehifar@manchester.ac.uk

ABSTRACT

In this paper, the process of encapsulating solid particle(s) into liquid droplets in a high-throughput flow-focusing microchannel is investigated numerically. Open source software is used, which computes fluid flow in an Eulerian framework and particle dynamics with a Lagrangian approach. Previous studies have demonstrated that if no action is taken, particles suspended in a liquid passing through a flow-focusing microchannel will be encapsulated at random. This is perhaps unsurprising, but in one such study, less than 35% of droplets were found to contain exactly one particle. The two aims of this study are (i) to explore the flow patterns arising in a microfluidic channel and (ii) to elucidate the effect of salient governing parameters on encapsulation efficiency (i.e., the fraction of droplets encapsulating one particle) by focusing on ordering the particles before reaching the droplet generation section. Following validation against experimental reference data, the capillary number is varied across the three droplet generation regimes: squeezing, dripping, and jetting. We demonstrate that under certain conditions, an encapsulation frequency of 100% can be achieved with ordered particles, but in most cases, this is significantly lower. We examine the flow field to help understand how this non-uniform distribution of particles occurs. Notably, we find the dripping to be the best option for particle encapsulation and in this case extend the study to explore the effect of junction angle, finding that an angle of 60° is the most favorable. Improved understanding of the encapsulation process derived from this study can help to improve design of high-throughput droplet generation microfluidic systems.

NOMENCLATURE

Abbreviations

CV	Coefficient of variation
ENPD	Expected number of particles per droplet
MP-PIC	Multiphase particle in cell
VOF	Volume of fluid

Greek letters

α	Phase volume fraction
α_{pm}	Close-packing volume fraction
θ	Junction angle (°)
κ	Interface curvature (m^{-2})
λ	Average number of particles/cells per droplet
μ	Viscosity (kg m^{-1} s^{-1})
ν	Dynamic viscosity (m^2 s^{-1})
ρ	Density (kg m^{-3})
σ	Surface tension (kg s^{-2})
τ	Stress tensor (kg m^{-1} s^{-2})
Φ	Particle distribution function

Symbols

A	Acceleration (m s^{-2})
Ca	Capillary number
C_D	Drag coefficient
d	Diameter or length (m)
$\bar{d}$	Average diameter (size) (m)
Dp	Drag function (s^{-1})
F	Force (N)
f	Frequency (s^{-1})
g	Gravity vector (m s^{-2})
h	Channel height (m)

N	Number of points adopted to discretize the channel width
n	Number of particles in a droplet
p	Pressure ($kg\,m^{-1}\,s^{-2}$)
Pp	Solid pressure constant ($kg\,m^{-1}\,s^{-2}$)
Q	Flow rate ($m^3\,s^{-1}$)
Re	Reynolds number
s	Particle spacing (m)
t	Time (s)
u	Velocity ($m\,s^{-1}$)
V	Volume (m^3)
w	Channel width (m)
x	Particle location in x-direction (m)
y	Particle location in y-direction (m)

Subscripts

c	Continuous phase
d	Dispersed phase
f	Fluid phase
L	Lift
p	Particle
pf	Fluid–particle interaction
r	Interface compression term

I. INTRODUCTION

The encapsulation of a solid particle into a liquid droplet of the volume of pico-to-nanoliters is an intriguing topic within contemporary microfluidic research. Emerged in the early 2000s, the main reason for its development is the application to a wide range of biochemical processes, including pharmaceutical synthesis,[1] toxicity studies,[2] protein detection,[3] and cell analysis and sequencing.[4]

Interestingly, a compelling yet challenging application is represented by the generation of droplets via high-throughput devices able to encapsulate solid particles. Approaches to droplet generation can be classified into passive and active methods.[5] The former relies on the inherent properties of fluids or materials to generate droplets without external energy input. These methods are generally based on physical phenomena or natural forces. The latter involves the application of external energy or forces to control and manipulate the formation of droplets.[6] Due to the complicated mechanisms and operations of active methods, passive methods are usually preferred.[7] Furthermore, when analyzing living cells,[8] external sources (e.g., electric field) could damage the cells irreparably.

In the present work, we use a passive flow-focusing microchannel, where two perpendicular inflow channels converge onto the primary channel, as shown in Fig. 1. Such an apparatus is employed regularly in droplet microfluidics.[9–11] The channels contain different fluids, such as water and oil, acting as continuous and dispersed phases, respectively. When the two reach the droplet-generating junction, the shear force promotes the formation of droplets of the dispersed phase, which may be able to capture one or more solid particles. As each droplet is isolated, it can serve as a microreactor and the behavior of the enclosed cells or particles can be studied. It should be pointed out that controlling the formation of droplets and the encapsulation process simultaneously in a high-throughput device can be a hard task.[12] In fact, channel geometry, flow rate, phase viscosities,

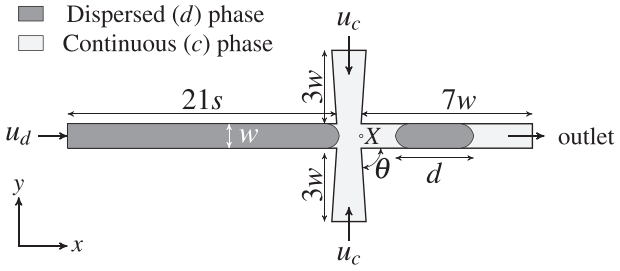

FIG. 1. Schematic illustration of the two-dimensional channel used in this study ($w = 230\,\mu m$). θ is equal to 87°. X is a probe located at the centerline and entrance of the main channel. u_c and u_d are inlet velocities of the continuous and dispersed phases, respectively. s is the particle spacing.

surface tension, wall wettability, and solid particle concentration play key roles in the droplet formation process.[13–18]

Apart from the possibility of generating droplets of a given size and frequency, significant attention has been devoted to controlling the number of particles trapped in each droplet. Amirifar *et al.*[4] recently reviewed the progress made in this field and stated that precise control of cells encapsulated in each droplet was a major challenge. Specifically, in single-cell studies, it is desired to reduce the number of empty droplets, as well as multiple encapsulations.[19,20] Those droplets may not be useful, which in the long term means a considerable waste of resources. In the case where no specific action is taken to the contrary, the process of particle encapsulation is expected to be completely random, and as such, the distribution of particles among droplets may be approximated by Poisson statistics as described by Edd *et al.*[19] They reported that for a stochastic process, the probability of a droplet encapsulating n particles can be predicted by $P(\lambda, n) = \lambda^n \exp(-\lambda)(n!)$, where λ is the average number of particles per droplet.[12,19] To minimize the droplets with $n \geq 2$, i.e., to avoid multiple encapsulations, the dispersed phase should be very dilute. This, in turn, increases the number of empty droplets. Statistically, less than 16% of droplets would have exactly one particle in them if multiple encapsulations are limited to 10%.[19]

The probability of the formation of droplets encapsulating exactly one particle can be effectively increased by ordering the particles prior to droplet formation.[19,20] Ordering the particles can be achieved by using inertial microfluidic channels, whereby a particle train can be formed before reaching the encapsulation section.[21–23] If particles are equally spaced, it follows that the frequency of their arrival at the flow-focusing junction will be constant. In practice, this is not quite true as the flow field associated with the droplet formation can impact particle spacing. In this paper, we begin by matching particle frequency to the droplet generation frequency, to achieve high encapsulation efficiencies up to 100%. So far, the controlled encapsulation process has been mostly studied experimentally.[8,16,20,24] Table I presents extracted data from some of the experimental works in droplet microfluidics encapsulating a range of particles and cells from large sizes, such as HeLa cells with a size of 15 to 21 μm, to small sizes, including Escherichia coli of 2 μm diameter.[25] As can be seen in Table I, when it comes to bacteria and fungus spores (i.e., below 10 μm in size), they must be encapsulated in large droplets (in the order of nanoliters) to provide enough space for growth during the incubation period.[26]

However, few efforts have been devoted to tackle the problem from a numerical viewpoint. To model the motion of particles in a

TABLE I. The size of channel, droplet, and particle/cell in experimental works reported in the literature.

Cell or particle size: d_p (μm)	Channel width: w (μm)	Droplet length: d (μm)	Cell or particle size/ droplet length: d_p/d (-)	Particle size/ channel width: d_p/w (-)	Ref.
20 (particle)	100	100–1000	0.02–0.2	0.2	Shahrivar *et al.*[20]
15 (particle)	25	45	0.33	0.60	Banerjee *et al.*[8]
10 (cell)	27	35	0.28	0.37	Edd *et al.*[19]
4 (cell)	230	370–440	~ 0.01	~ 0.02	Beneyton *et al.*[16]
~ 3 (cell)	75	225	~ 0.01	~ 0.04	Wang *et al.*[26]
2 (cell)	~ 60	60	0.03	~ 0.03	Yu *et al.*[25]

flow, two approaches are available: Eulerian–Eulerian and Eulerian–Lagrangian. The interested reader can refer to the work by Heinrich and Schwarze,[27] who compared the two methods for a spray atomization case, for further insights and a discussion about the superior accuracy of the latter. The numerical simulation of solid particle motion in a multiphase flow requires the coupling of different methods. The first study on droplet encapsulation was done by Yang[28] in 2013. They added one soft cell to the domain and simulated its deformation as it passed the droplet microfluidic channel for one dripping case. They used the lattice Boltzmann method coupled with the immersed boundary method and reported that the small-sized particles have a negligible effect on the encompassing fluid dynamics. Recently, the finite element method using COMSOL Multiphysics software was successfully adopted to simulate the rigid particle movement in droplet microfluidics by Yaghoobi *et al.*[29] They focused on pairing efficiency for two types of particles and examined the effects of the walls, liquid–liquid interface, and particle spacing on the co-encapsulation and found that the encapsulation was very sensitive to the latter. Outokesh *et al.*[30] evaluated the encapsulation of many small magnetic particles in every droplet in the presence of a magnetic field and focused on the enrichment of the particles by splitting the droplets.

In this work, we aim to provide further insight on improving the control over particle encapsulation process through a proper arrangement by numerical simulations. Specifically, we aim to capture a single solid particle within a single fluid droplet in a high-throughput channel so that hundreds of droplets with exactly 1 particle in them can be produced. This would minimize the formation of empty droplets as well as droplets with two or more particles in them that are not favorable in practice and are considered as waste. Our analyses are carried out by adopting OpenFOAM to model a cross-junction channel in which droplets are passively formed. We prescribe that the particles are uniformly spaced when reaching the cross-junction and evaluate the impact of this choice on the efficiency of the encapsulation process. The rest of the paper is organized as follows. First, the problem is stated, and the numerical solver is discussed in Sec. II. Second, the solver is tested against experimental findings in Sec. III. Third, the effect of particle spacing on the efficiency of encapsulation is evaluated for three common droplet generation regimes, namely, squeezing, dripping, and jetting in Sec. IV. Eventually, some conclusions are drawn in Sec. V.

II. PROBLEM STATEMENT AND NUMERICAL METHODS

In this section, first the problem is stated. Then, the salient features of the adopted numerical solvers are outlined.

A. Problem statement

Making reference to Fig. 1, a two-dimensional cross-junction channel, similar to the geometry used by Beneyton *et al.*,[16] with width $w = 230\ \mu$m is considered. A dispersed (aqueous) phase is injected from the left inlet section with velocity u_d, while a continuous (oil) phase enters from the top and bottom inlets with velocity u_c. The rightmost section is treated as an outlet. Walls are considered as no-slip boundary conditions with a contact angle of 160°. Particle size, d_p, and density, ρ_p, are set to fixed values equal to 4×10^{-6} m and 230 kg/m^3, respectively. All the mentioned values are representative of actual cases used by Beneyton *et al.*[16] The length of oil inlets is $3w$, allowing the flow to become fully developed before reaching the junction. The aqueous phase inlet should be long enough to accommodate 20 particles. Other relevant geometric characteristics are reported in Fig. 1. The length of the main channel is set to be $7w$, which is long enough to capture the droplet breakup and formation. θ is equal to 85°. The problem is governed by the incompressible Navier–Stokes equations. These are coupled to the volume-of-fluid (VOF) method to track the interface between the two fluids. Moreover, the multiphase particle in cell (MP-PIC) is adopted to model particle–fluid and particle–particle interactions. VOF and MP-PIC methods are discussed in the following.

B. VOF method

Let us consider the presence of two fluids, namely, fluid 1 and fluid 2. The liquid–liquid interface can be tracked using the VOF method. First, the summation of all volume fractions should be equal to 1,

$$\alpha_p + \alpha_f = 1, \tag{1}$$

where α_p is the particle phase volume fraction, and α_f is the fluid phase volume fraction. If fluid 1 is the continuous phase and fluid 2 is the dispersed phase, we can calculate α_f using

$$\alpha_f = \alpha_{fluid_1} + \alpha_{fluid_2} = \alpha_c + \alpha_d. \tag{2}$$

The continuity and momentum equations, respectively, are

$$\frac{\partial \alpha_f}{\partial t} + \nabla(\alpha_f u_f) = 0, \tag{3}$$

$$\frac{\partial(\rho_f \alpha_f u_f)}{\partial t} + \nabla \cdot (\rho_f \alpha_f u_f u_f) = -\alpha_f \nabla p + \nabla \cdot (\alpha_f \tau_f) + \alpha_f (g \nabla \rho_f) + F_\sigma - F_{pf}, \tag{4}$$

where u_f is the fluid phase velocity, p is the fluid pressure, τ_f is the fluid stress tensor, g is the gravity vector, ρ_f is the density of the fluid, F_σ is

the surface tension force, and F_{pf} is the fluid–particle interaction force. ρ_f must be calculated with respect to each fluid phase volume fraction as

$$\rho_f = \alpha_c \rho_c + \alpha_d \rho_d. \tag{5}$$

F_σ is calculated as

$$F_\sigma = \sigma \kappa \frac{\partial \alpha_c}{\partial \alpha_f}, \tag{6}$$

where κ is the curvature and is approximated as

$$\kappa = -\frac{\partial}{\partial x_i}\left(\frac{\partial \alpha_c / \partial x_i}{|\partial \alpha_c / \partial x_i|}\right). \tag{7}$$

The phase tracking equation is

$$\frac{\partial \alpha_f \alpha_c}{\partial t} + \nabla \cdot (\alpha_f \alpha_c u_f) + \nabla \cdot \left[\alpha_f \alpha_c (1 - \alpha_c) u_r\right] = 0, \tag{8}$$

u_r is the interface-compression velocity and is only active in the interface between the two fluids where α_c is neither 0 nor 1. More details on the VOF method can be found in our previous work.[14] The last term at the right-hand side of Eq. (4), F_{pf}, represents the fluid–particle interaction forces and is further discussed in Sec. II C.

C. MP-PIC method

The MP-PIC model developed by Andrews and O'Rourke[31] is used to represent collisions without the need to directly resolve particle–particle interactions to reduce computational costs. Specifically, the *MPPICInterFoam* solver in *OpenFOAM*-v2012 is employed. The bridge between the Lagrangian discrete particle and the Eulerian grid is represented by the particle distribution function, $\phi(x_p, u_p, \rho_p, V_p, t)$, which represents the possibility of having a particle at location x_p and time t having a velocity of u_p, density of ρ_p, and volume of V_p. ϕ is defined using the Liouville equation,[32–34]

$$\frac{\partial \phi}{\partial t} + \nabla_x \cdot (\phi u_p) + \nabla_{u_p} \cdot (\phi \cdot A_p) = 0, \tag{9}$$

where A_p is the particle acceleration and is calculated as

$$A_p = \frac{\partial u_p}{\partial t} = D_p(u_f - u_p) - \frac{1}{\rho_p}\nabla p + g - \frac{1}{\alpha_p \rho_p}\nabla \tau_p \tag{10}$$

with

$$D_p = C_D \frac{3}{8}\frac{\rho_f}{\rho_p}\frac{|u_f - u_p|}{0.5 d_p}. \tag{11}$$

Here, C_D is the drag coefficient exerted by the continuous phase, and τ_p is the particle stress tensor and indicates the collision of the particles. When calculating A_p, the three terms on the right-hand side represent the effects of drag force, particle–fluid interaction, and particle–particle interaction, respectively. The drag coefficient is calculated according to the Wen–Yu model,[32,35] that is

$$C_D = \begin{cases} \frac{24}{Re_p}\alpha_c^{-2.65}(1 + 0.15(\alpha_c Re_p^{0.687})) & \text{if } Re_p < 1000, \\ 0.44\alpha_c^{-2.65} & \text{if } Re_p > 1000, \end{cases} \tag{12}$$

where

$$Re_p = \frac{\rho_f (u_f - u_p) d_p}{\mu_f}, \tag{13}$$

and d_p is the particle diameter. τ_p represents the average collision force on the particles,

$$\tau_p = -p_p + (1 - \alpha_p)\mu_p \nabla u_p, \tag{14}$$

where the particle phase viscosity μ_p is considered constant, and its pressure is calculated by

$$p_p = P_p \frac{\alpha_{pm} - \alpha_p}{(1 - \alpha_p)^2}. \tag{15}$$

Here, P_p is the solid pressure constant, α_{pm} is the particle volume fraction at packing limit, and α_p is computed on the Eulerian grid and is a function of the particle distribution function ϕ, i.e.,

$$\alpha_p = \iiint \phi V_p \cdot dV_p \cdot d\rho_p \cdot du_p. \tag{16}$$

To couple the Lagrangian grid and the Eulerian one, the interphase momentum transfer function is needed and it can be calculated by

$$F_{pf} = \iiint \phi V_p \rho_p \left[C_D(u_f - u_p) - \frac{\nabla p}{\rho_p}\right] dV_p \cdot d\rho_p \cdot du_p. \tag{17}$$

To calculate F_{pf}, two velocities, i.e., u_f and u_p, are required. The former is achieved by interpolating the fluid velocity on the Eulerian grid. u_p is the particle mean velocity and is given by

$$u_p = \frac{1}{\alpha_p \rho_p}\iiint \phi V_p \rho_p u_p \cdot dV_p \cdot d\rho_p \cdot du_p, \tag{18}$$

and α_p and F_{pf} can be mapped on the Eulerian grid.

We conclude this section by discussing the computation of particle–fluid interaction. These are drag, buoyancy, and pressure gradient, as well as other forces such as virtual mass, Basset, Saffman, and Magnus forces. Drag and pressure gradient forces are only relevant to the particle dynamics and are calculated as

$$\text{drag force:} \quad F_d = C_D(u_f - u_p), \tag{19}$$

$$\text{pressure gradient force:} \quad F_p = -\frac{\nabla p}{\rho_p}, \tag{20}$$

while any other force contribution is disregarded.

III. VALIDATION

The adopted approach is validated against the experimental findings in the work by Beneyton *et al.*[16] They suggested controlling the average number of spores encapsulated in droplets, namely, λ, by adjusting the concentration of the spore at the dispersed phase inlet. They used a microchannel with a cross section of $230 \times 230\,\mu m^2$ to generate 10–20 nl droplets with a frequency of 80–90 droplets per second. In their setup, the oil phase is HFE-7500 with $\rho_{oil} = 1630\,kg/m^3$ and $\nu_{oil} = 0.8 \times 10^{-6}\,m^2/s$. The aqueous phase is water with $\rho_{water} = 996\,kg/m^3$ and $\nu_{water} = 1 \times 10^{-6}\,m^2/s$. The surface tension value is not indicated in their work, but it is stated that a surfactant is added to the oil phase to reduce the surface tension between the two liquid

TABLE II. Values of the droplet size, d (μm), for different grids in two-dimensional analyses. *N* is the number of points adopted to discretize *w*. Cases 1 and 3 refer to scenarios in Beneyton *et al.*[16] work.

	Mesh	Cells per w (N)	Wall refinement?	d_sim (μm)	d_exp (μm)	Error (%)
Case 1 ($Q_{oil} = 10\ \mu$l/h; $Q_{water} = 3\ \mu$l/h)	M1	15	No	340	362	6.0
	M2	23	No	359		0.9
	M3	46	No	365		0.9
	M4	46	Yes	365		0.9
	M5	69	No	370		1.9
	M6	69	Yes	369		1.7
Case 3 ($Q_{oil} = 5\ \mu$l/h; $Q_{water} = 4.6\ \mu$l/h)	M1	15	No	470	480	2.1
	M2	23	No	500		4.2
	M3	46	No	510		6.3
	M4	46	Yes	509		6.0
	M5	69	No	516		7.5
	M6	69	Yes	514		7.1

phases and consequently to increase the stability of droplets. We test different values of the surface tension coefficient, i.e., $0.01 \leq \sigma \leq 0.04\,\mathrm{N/m}$, which according to the literature correspond to cases with surfactant involved, and realize that the case with $\sigma = 0.015\,\mathrm{N/m}$ generates similar results to Beneyton *et al.*'s experiments. Hence, in our simulations, we use this value for the surface tension. The same geometry as Beneyton *et al.*[16] is created and meshed. A different number of grid points discretizing *w* varying from 15 to 69 is tested, and results are reported in Table II. Meshes M1, M2, M3, and M5 are uniform, while M4 and M6 have near wall refinement. By testing the flow rates corresponding to the smallest and largest droplets in Beneyton *et al.*[16] work, it is found that at least 23 points are needed to minimize the effect of mesh cells on the droplet size while having reasonable liquid–liquid interface thickness. To assess the impact of near-wall mesh refinement, the cell adjacent to the wall is refined by a factor of 5 in M4 and M6. Figure 2 depicts the uniform mesh used in this study with 23 cells per *w*. By comparing the droplet sizes in all cases, we find that near-wall refinement has no significant effect on the results. This corroborates conclusions by Li *et al.*,[10] for a similar range of flow parameters. It is important to note that there are conflicting requirements for mesh resolution when using the present Eulerian–Lagrangian framework. As expected, the finite volume based VOF solver will converge to a grid independent solution with decreasing grid size. However, the Lagrangian solver requires that the Eulerian grid dimension is larger than the particle size, such that each particle

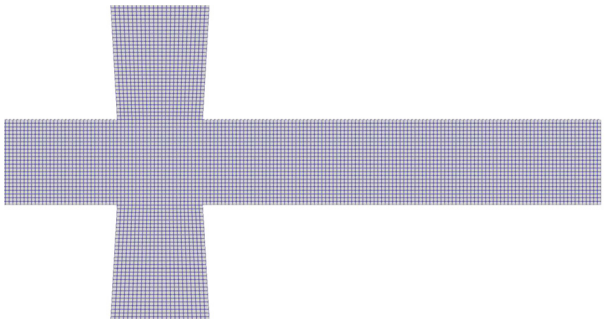

FIG. 2. Simulation domain discretized using mesh M2, with 23 grid points per width, without near wall refinement.

can fit within a single grid cell. In the present work, the particle size is 4 μm and so a grid size of 3 μm (as for M5) is impractical. The use of M2 with grid size of 10 μm is a reasonable compromise.

The three scenarios devised in Beneyton *et al.*[16] are simulated using *MPPICInterFoam*. A comparison in terms of droplet volume and frequency is shown in Table III. We find that the droplet volume is in good agreement with the experimental data, and the maximum error is 5%. The droplet frequency error for cases 1 and 2 is below 10%. For case 3 that has much larger droplets, the measured error increases to 19%, due to the occurrence of errors associated with the interface, so-called parasitic currents. In the present configuration, larger droplets are generated by significantly reducing the channel flow rates. Lower resulting velocities are impacted to a greater degree by the presence of errors associated with these errors. By acknowledging that *MPPICInterFoam* is able to capture the droplet volume accurately, but exhibits non-negligible errors in the frequency computation of very large droplets; in the following, we restrict our focus to cases where the droplet length is less than $2w$, such that the error associated with this phenomenon is expected to remain below 10%.

Different concentrations of particles are introduced in the channel to see how the number of spores per drop changes. For spore concentration in the aqueous inlet equal to 5, 10, and 15 spores per microliter, the reference data reported that $0.1 \leq \lambda \leq 0.3$. Using the same three spore concentrations, we find that the values of λ obtained by our simulations are also $0.1 \leq \lambda \leq 0.3$, which is very well placed within the expected range.

IV. RESULTS AND DISCUSSION

We now turn our attention to the simulation results of particle-encapsulating droplets in a cross-junction device. The same geometry is used as for the validation section, i.e., as depicted in Fig. 1. Let us

TABLE III. Comparison of simulation results with Beneyton *et al.*[16] experiments.

			Droplet volume (nl)			Droplet frequency (Hz)		
Case	Q_{oil} (ml/h)	Q_{water} (ml/h)	Experiment	Simulation	Error	Experiment	Simulation	Error
1	10	3	10	9.9	1%	80	72	10%
2	8	6	18	18.5	2.7%	90	82	9%
3	5	4.6	20	21	5%	90	76	19%

recall that this work focuses on increasing the chance of trapping exactly one particle per droplet using particle pre-ordering. In this section, simulation results of particle-encapsulating droplets in a cross-junction device are reported and the effect of particle spacing is discussed in different droplet generation regimes. The full set of flow scenarios simulated in this section is listed in Table IV. We do not consider the process of ordering the particles upstream of the junction. Instead, we assume that all particles are ordered before reaching this point, achieved by predefining the position of each particle within the entry section of the channel.

In inertial microfluidics, particles undergo shear-gradient and wall-induced lifts. The resultant force governs the particle location, and it depends on the Reynolds number, $\mathrm{Re} = \frac{\rho u D}{\mu}$, and on the ratio d_p/w. When $\mathrm{Re} < 80$, the lift is calculated by $F_L^I \approx \rho u^2 d_p^3/w$ at the center of the channel.[36] In all our cases, Q_d is constant and equal to $1.667 \times 10^{-9}\ \mathrm{m^3\ s^{-1}}$. At the dispersed phase inlet channels, $\mathrm{Re}_d < 10$ and particle size is 4 μm, resulting in negligible lift force in the order of 10^{-15} N, which explains the persistence of particles at the centerline as they move toward the junction. This is in agreement with Kwon *et al.*,[37] thus supporting our assumption of using preordered particles.

For the purpose of this study, we will assume that all particles are pre-ordered along the channel centerline, upstream of the cross junction. This is a convenient assumption since the practical implementation of particle ordering is known to depend on the specific setup of the micro-channel, and different particle equilibrium positions are observed in different circumstances. For instance, Prohm and Stark[38] demonstrated that particles positioned along the centerline are unstable in a rectangular channel, and the particle/channel confinement ratio is known to determine stability. Nevertheless, it has been shown by Di Carlo *et al.*[39] that ordering along a channel centerline can be achieved, for example, by using a spiral inertial channel to focus particles upstream of the cross junction,[39] which is, thus, analogous to the assumption we have made. Further study is needed to quantify the impact (adverse or favorable) of different equilibrium positions on particle path, velocity, and encapsulation efficiency.

In microfluidic droplet formation, changing the capillary number, $\mathrm{Ca} = \mu_c u_c/\sigma$, alters the droplet generation frequency. Thus, the space between particles, s, should be modified so that the droplet generation frequency is close to the particle injection frequency. To evaluate such effect, different cases are simulated by varying Ca and s in the range of $0.005 < Ca < 0.03$ and $100 < s < 800$ μm, respectively. The relative frequency of droplets with 0, 1, or 2 particles in each droplet is examined. The values reported in this work account for the injection of 20 particles into the channel in each case. Thus, the simulation time depends on Ca and s. In all simulations, the Courant number is set to be below 0.3, thus leading to a time step, which varies between 2×10^{-6} and 7×10^{-6} s. To account for the transient effect at the beginning of the simulations, the first two particles are excluded from the analyses.

A. Squeezing

When considering the squeezing regime, the continuous phase velocity is very low and the dominant force forming the droplet is the pressure one. Different stages of droplet formation are shown in Figs. 3 and 4.

In Fig. 3, at stage 1, the dispersed phase thread penetrates the continuous phase and starts to fill the channel width. Consequently, the cross-junction area available for the continuous phase reduces, causing u_c to increase, as shown in Fig. 3(a). Note that two weak circulation areas are experienced at the tip of the thread, which are due to flow obstruction by the higher velocity continuous phase. At stage 2, the cross junction is fully blocked by the dispersed phase causing a pressure buildup and reaching a maximum pressure, which forms the droplets. As evident in Fig. 3(b), due to channel blockage, u_d reduces. The pressure buildup is now strong enough to push the liquid–liquid interface away and initiates the necking stage. At the neck, u_d is high due to the thinness of this region, giving the disperse phase a limited passing area. Then, the thread becomes progressively thinner until it reaches a critical point and breaks. As shown in Fig. 3(c), at stage 3 (i.e., right after detachment), four circulation areas are detected. Two at the tip of the thread formed due to retraction of the interface, i.e., interface moves toward the inlet, while the dispersed phase is trying to advance. Simultaneously, the droplet is pushed forward causing two other vortices at the continuous phase. Interestingly, Soh *et al.*[40] analyzed the flow in a T-junction and reported two circulation areas at pinch-off, one at the retracted tip and one at the detachment location, adjacent to each other. Here, for the cross-junction geometry, we report two circulation areas slightly apart. At stage 4, the droplet is fully formed and at equilibrium. It moves toward the outlet having the same velocity as the continuous phase. Thus, the two circulation areas adjacent to the droplet disappear. On the other hand, the tip of the thread is still recoiling and has not reached equilibrium. The two vortices become larger, inducing two new counter-rotating vortices before the junction, see Fig. 3(d). When the thread stops retracting and starts moving forward again (stage 1), all vortices disappear.

The circulation areas and streamlines dictate the particle locations and velocity. For instance, at stage 3, if a particle is trapped in the upper circulation areas right before detachment, it ends up being in

TABLE IV. Summary of cases examined in the present study.

Regime	Ca	s (μm)	Θ
Squeezing	0.005	200, 300, 400, 500, 600, 700, 800	85°
	0.01	200, 300, 400, 500, 600, 700, 800	85°
Dripping	0.015	200, 250, 275, 300, 325, 350, 400, 500, 600, 700, 800	85°
	0.02	100, 150, 175, 200, 225, 250, 300, 400, 500, 600, 700, 800	85°
	0.02	200	30°, 60°, 90°, 120°, 150°
Jetting	0.025	50, 100, 150 200, 250, 300	85°
	0.03	50, 100, 150, 200, 250, 300	85°

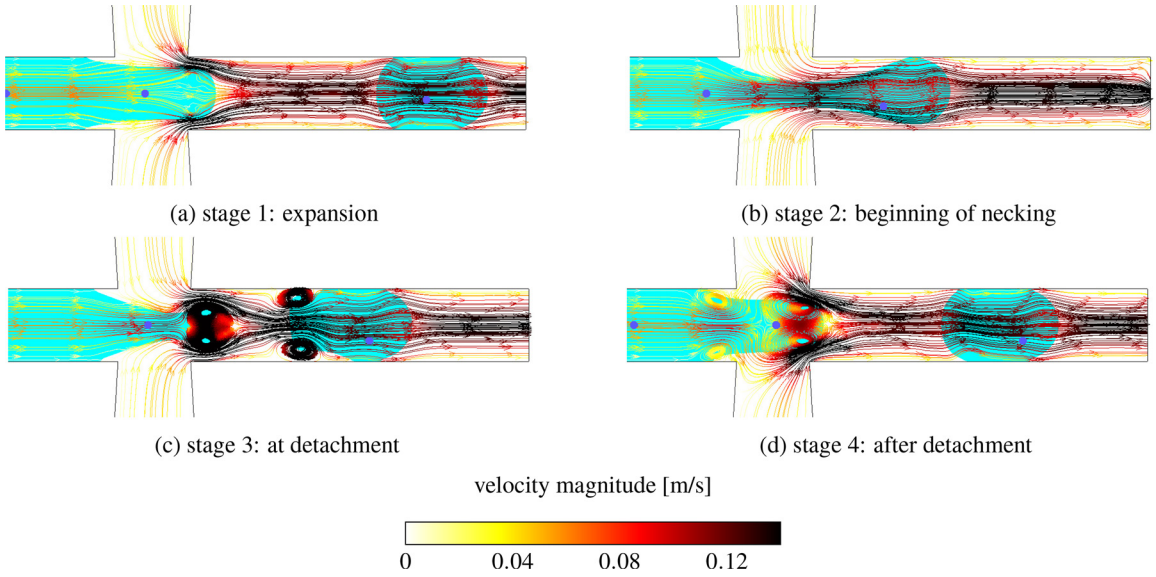

FIG. 3. Squeezing: different stages of droplet formation. The cyan color represents the dispersed phase.

the upper half of the droplet and vice versa. The location of particles in the droplet then dictates the velocity of the particle, which is further explained in Sec. IV B 1. At stage 4, if a particle reaches a junction while strong circulation areas are present at the tip of the dispersed phase [due to recoiling, see Fig. 3(d)], the particle would linger at the junction for a while (until circulations disappear) and cannot enter the high-speed circulation areas. This allows the next particle to reach the junction as well and, eventually, results in multiple encapsulations. Furthermore, in some instances, particles move with very high velocities. In biochemical applications, if cells go through a high-speed environment they might deform and lose their viability.[41] Thus, when designing the microfluidic droplets, the maximum allowed velocity in the necking area should also be taken into account.

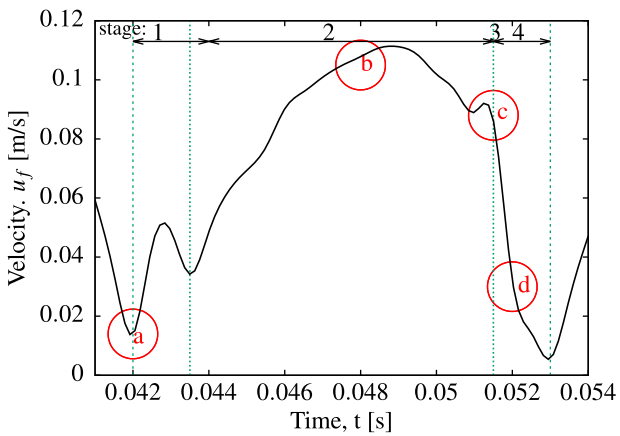

FIG. 4. Squeezing: velocity magnitude at probe X at different stages; stage 1: expansion; stage 2: necking; stage 3: at detachment; and stage 4: after detachment; and a to d represent the instants shown in Fig. 3.

Different speeds arise at different stages. Figure 4 shows the speed and duration of each stage for one droplet formation cycle at the centerline of the right-hand side channel entrance, probe X, which is shown in Fig. 1. The necking stage specifically takes longer than other stages, while detachment is just an instance. When the droplet detaches and the system reaches equilibrium, the velocity drops to a minimum.

In Fig. 5, the effect of the particle spacing s on the occurrence of a specific number of particles per droplet is sketched. At Ca $= 0.005$, for $s = 500\,\mu$m, droplet frequency and particle frequency fully synchronize and particle encapsulation efficiency reaches 100%. Spacing smaller than 500 μm results in the formation of droplets with two particles. On the other hand, $s > 500\,\mu$m causes the presence of empty droplets. By increasing Ca to 0.01, the maximum relative frequency of 93% is achieved when $s = 400\,\mu$m. Any spaces beyond that enhance the chances of having empty droplets, while any smaller spacing causes the emergence of droplets with two particles. Interestingly, at $s = 200\,\mu$m, 95% of the droplets encapsulate exactly two particles.

In squeezing, the droplets are large, and their size depends on the channel constraints. Larger droplets mean lower droplet generation frequency. As for the encapsulation, the distance between particles should be wide enough to allow particle frequency to be synchronized with the droplet generation one.

B. Dripping

A further increase in Ca causes the generation regime to change from squeezing to dripping. The shear stress becomes the dominant force dragging the liquid thread forward, while the pressure forces become negligible. Different stages of droplet formation are illustrated in Fig. 6. Stage 1 is the expansion of the dispersed phase. At the end of stage 1 and right before the beginning of stage 2, two weak circulation areas are formed at the tip, which are caused by the higher velocity continuous phase obstructing the flow. These two circulations are

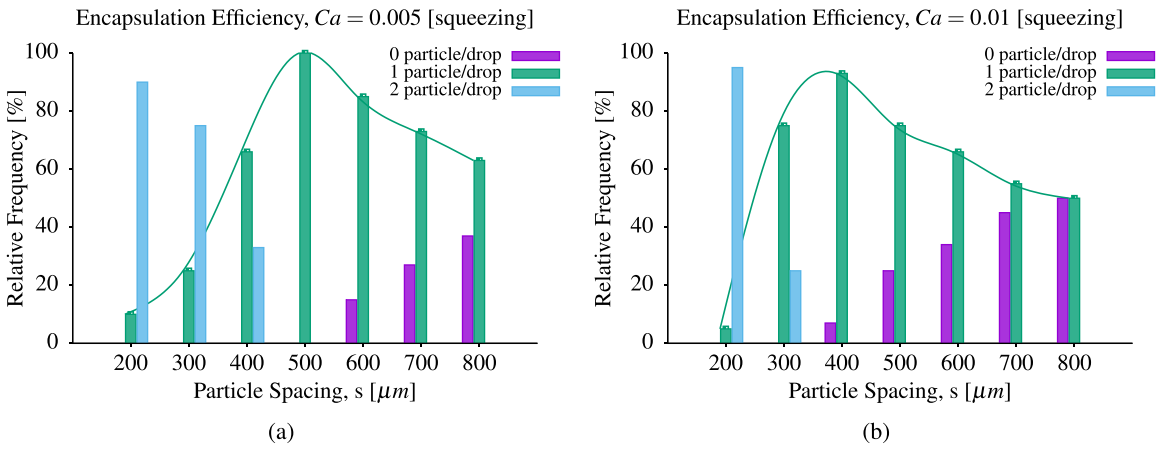

FIG. 5. Squeezing: effect of particle spacing on particle encapsulation at (a) Ca = 0.005 and (b) Ca = 0.01.

stronger than those created in the squeezing regime at a similar stage. Owing to stronger shear force, the necking stage (stage 2) starts earlier than squeezing before the channel is fully obstructed. The start of necking can be identified by the interface being pushed toward the centerline, followed by a change in interface curvature. Similar to squeezing, u_d in the neck is higher compared to other regions of the dispersed phase. As the necking starts, the small circulation areas detected at stage 1 disappear. At stage 3, when the shear stress becomes strong enough, droplet pinch-off occurs. Here, channel blockage does not happen; thus, large high-pressure zones are not seen. Also, at the detachment, no strong circulations are detected. At stage 4, the droplet reaches equilibrium and travels at the same velocity as the bulk. Yet, similar to squeezing the tip of the thread moves backward—due to surface tension—causing two large circulation zones, which consequently induce the formation of two smaller circulation zones right before the junction edges. Kalli *et al.*[42] reported only two circulation areas at pinch-off, and the difference might be a result of edge shape as their cross-junction has oval edges.

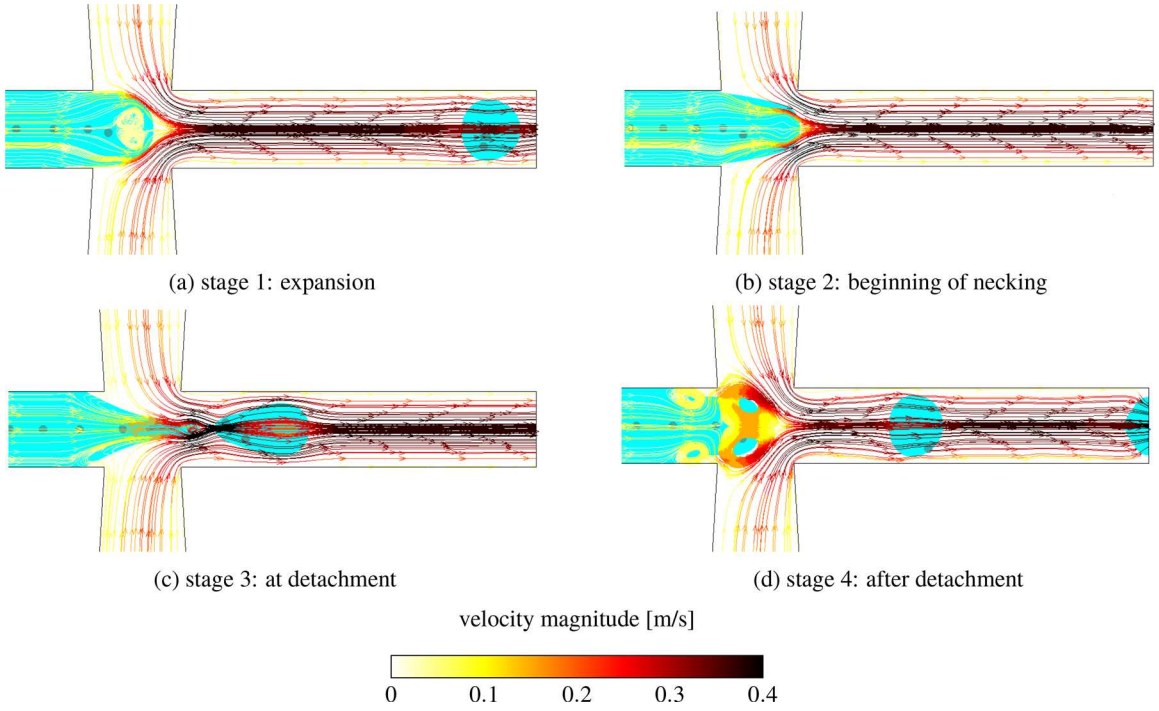

FIG. 6. Dripping: different stages of droplet formation. The cyan color represents the dispersed phase.

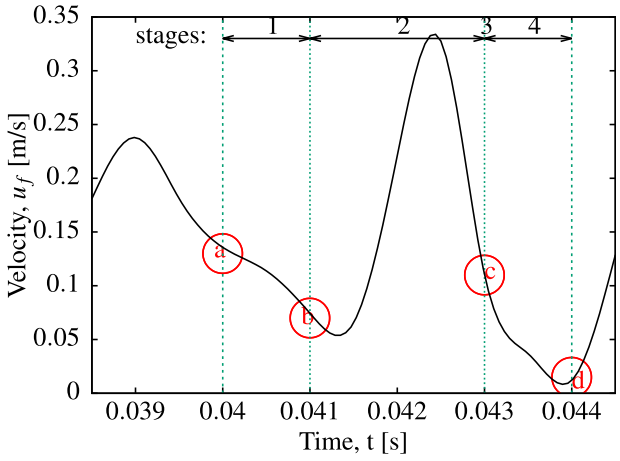

FIG. 7. Dripping: velocity magnitude at probe X at different stages of droplet formation; stage 1: expansion; stage 2: necking; stage 3: at detachment; and stage 4: after detachment; and a to d represent the instants shown in Fig. 6.

Different stages occur at different speeds as illustrated in Fig. 7. In squeezing, we reported a relatively long necking stage. However, in dripping, drops are detached and formed faster due to stronger shear stress, so the necking stage does not take as long. Furthermore, the velocity gradient during necking is higher compared to squeezing and a sharp peak is seen in Fig. 7. After detachment, at the end of stage 4, velocity decreases to a minimum representing the equilibrium state and the end of the cycle.

A closer look at flow physics is instrumental to a better understanding of the particles' fate. Particles are light, and the Reynolds number of the flow is very low, so they tend to follow the streamlines. At stage 1 [see Fig. 6(a)], the two small circulations at the tip push the closest particle away, causing the spacing between the first and second particles to reduce. Until those two vortices disappear, the particles stay at the same location, as shown in Fig. 6(b). Then, as the necking starts and u_d increases, the particles rapidly move forward and become encapsulated in the forming droplet [see Fig. 6(c)]. Here, the particle spacing is much smaller than squeezing to ensure high encapsulation efficiencies. As shown in Fig. 6(d), the next two particles, which were already very close to the junction due to small spacing, have now entered the junction and get trapped in the emerging circulations. The particles end up either in the upper or lower large circulations, which eventually dictate particle location inside the droplet. This is further explained in Sec. IV B 1.

In this regime, droplets smaller than the channel width are formed and the droplet frequency is higher than squeezing. Thus, lower particle spacing compared to squeezing results in a higher relative frequency of one particle per droplet. As shown in Fig. 8(a), at $s = 200\ \mu$m, 96% of the droplets encapsulate exactly one particle. 198 droplets are generated per second, of which 96% capture one particle. When compared to the squeezing regime, the efficiency of the system (i.e., the fraction of droplets encapsulating one particle) is larger. One point to be wary of is the rapid shift in relative frequencies compared to the squeezing regime. Changing s from 200 to 100 μm results in a drastic change in the relative frequency as suddenly 93% of the droplets have two particles. When increasing the flow rate, the sensitivity of encapsulation also increases and more precautions are required.

Overall, we find that the dripping regime is the most suitable for this application as it offers good compromise between flow rate and control over the encapsulation process and potential to achieve a high rate of production of monodispersed droplets. This is in agreement with other reports.[43,44] As such, we have extended the analysis in this section, as follows.

1. Particle path

In this section, the paths of particles are discussed by setting Ca = 0.02 and $s = 400\ \mu$m. In a confined channel with no-slip wall boundary condition, there is a velocity gradient in the fluid domain, including within the droplets.[42,45] The effect of velocity gradient on particle velocity is discussed here. The horizontal location of particles along the channel from the moment they reach the junction, time step 1, until they leave the channel, time step 6, is plotted in Fig. 9. The slope of the curves represents the velocity of particles. Not all particles have similar speeds as their velocity depends on their location in droplets. Particles 1 and 4 that are at the center of the channel have higher

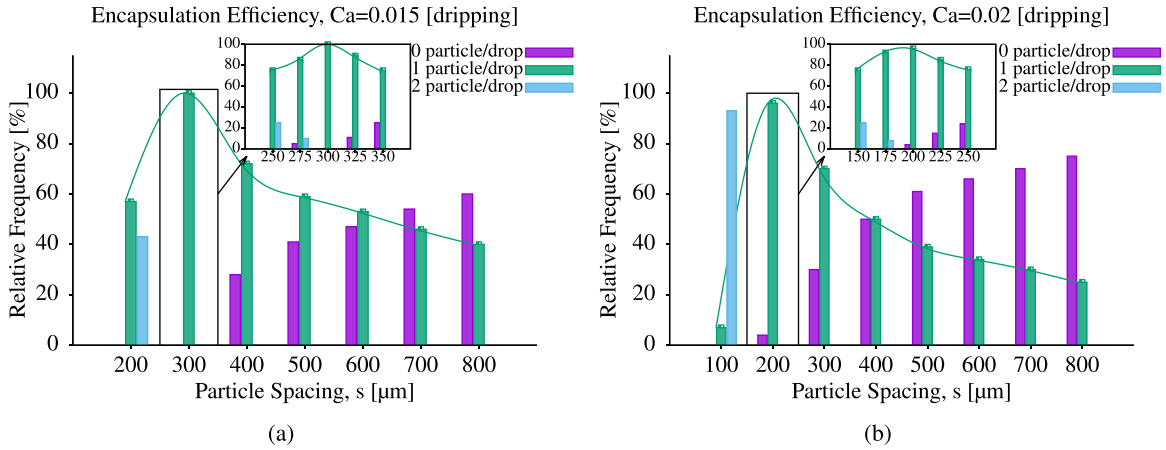

FIG. 8. Dripping: effect of particle spacing on particle encapsulation at (a) Ca = 0.015 and (b) Ca = 0.02.

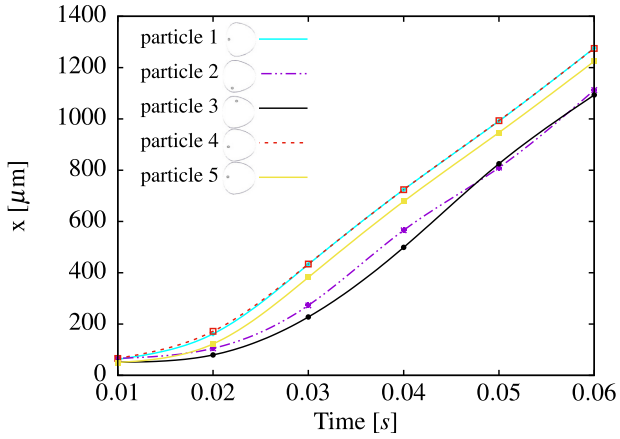

FIG. 9. Dripping: particle location in time for Ca = 0.02 and $s = 400\ \mu$m. The time for each particle starts from the moment it enters the main channel.

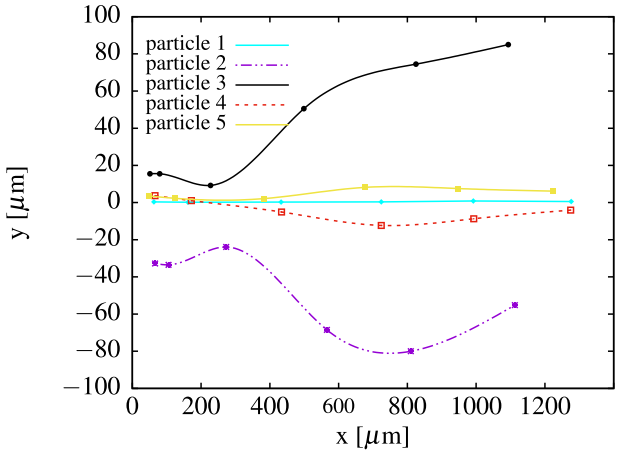

FIG. 10. Dripping: particle locations as they pass the main channel for Ca = 0.02 and $s = 400\ \mu$m.

velocities, while particles 2 and 3 that are near the channel walls have lower velocities.

Moreover, to visualize the 2D path particles take as they move forward, Fig. 10 is plotted. The distribution of particles between these locations appears to depend on Ca and s. We observe three different positions within the droplet: close to the upper wall (particle 3), near the centerline (particles 1, 4, and 5), or close to the lower wall (particle 2). It is clear that the position of the particle at the point of droplet formation dictates its resulting position within the drop. If the particles are spaced too close to one another, they are more likely to interact with the vortex system resulting from the upstream droplet formation. Particles that do not interact with the upstream vortex tend to remain along the centerline, while particles that do interact are observed to move toward the channel walls. The direction of this movement (either up or down in this study) depends on whether the particle interacts with the upper or lower vortex; it ends up in the corresponding location within the droplet downstream.

2. Effect of junction angle

In this section, we explore the effect of junction geometry on particle encapsulation as well as droplet formation. So far, we found that the dripping regime not only generates monodispersed droplets as also reported by other authors,[43,44] but also allows excellent control over the encapsulation process so that all formed droplets would have 1 particle in them. Let us adopt this regime for further tests.

We investigate how the junction angle, θ, affects the droplet size and monodispersity. As shown in Fig. 11(a), for Ca = 0.02 and $s = 200\ \mu$m, when $\theta \leq 90°$, the droplets are highly monodispersed and the coefficient of variation (CV), i.e., standard deviation over mean value, is below 0.5%. Any increase beyond 90° has a negative effect, with $\theta = 150°$ having the highest value of CV equal to = 2.5% and a flatter distribution curve. Furthermore, increasing θ results in smaller droplets. A variation of θ affects the directions of streamlines too. When $\theta \leq 90°$, the two phases' streamlines at the junction move in opposite directions. This affects the interfacial forces and drag forces and, consequently, droplet size.

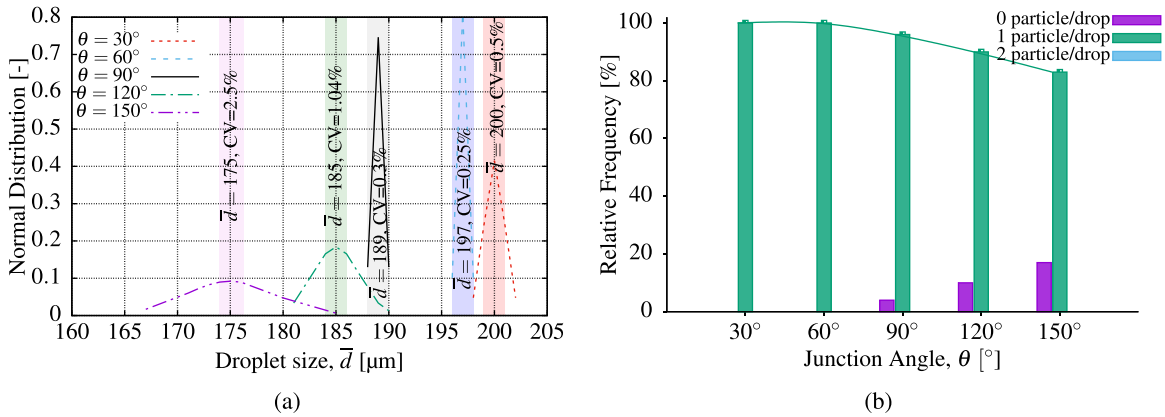

FIG. 11. Dripping: effect of junction angle on (a) D and monodispersity of droplets and (b) particle encapsulation efficiency, at Ca = 0.02 and $s = 200\ \mu$m.

In Fig. 11(b), the effect of θ on particle encapsulation is illustrated. Interestingly, $\theta \leq 60^\circ$ caused the relative frequency of 1 particle/drop to decrease and enhance the formation of empty droplets. To explain the adverse behavior, let us highlight that the encapsulation efficiency is directly related to the droplet size as depicted in Fig. 13(b). Moreover, larger θ forms smaller droplets, meaning that droplet frequency increases, while particle frequency remains constant. Taking both into account, by increasing θ, droplets would detach sooner, so particles would not have enough time to pass the junction and accompany the droplet. We find that the optimum value of the junction angle is $\theta = 60^\circ$, because (i) the droplets are highly monodispersed and (ii) almost all droplets trap exactly one particle.

C. Jetting

The third regime, jetting, occurs at Ca $\geq$ 0.025. Similar to dripping, the competition between viscous force and surface tension generates the droplets. Increasing u_c, thus increasing Ca, enhances the shear stress. According to Zhou *et al.*[46] and Fu *et al.*,[47] the pinch-off mechanism in the jetting regime is similar to that in the dripping regime. We have also detected similar behavior and mechanism between the two regimes. To avoid repetition, different stages are not depicted here. To study the encapsulation of particles, first, droplet sizes should be investigated. In jetting, the breakage of a liquid jet generates droplet, i.e., Rayleigh–Plateau instabilities.[6] Thus, a main characteristic of the jetting regime is the generation of droplets with different sizes. Different droplet size means different detachment time for each droplet size. Thus, synchronizing the droplet frequency with particle frequency becomes a hurdle. Figure 12 illustrates the particle encapsulation for two different Ca. At moderate velocities, the highest single encapsulation efficiency was 90% for $s = 150\,\mu$m. This is possible because formed droplets were only of two sizes, $d_1 = 124\,\mu$m and $d_2 = 179\,\mu$m, with a difference in size being not so large. So, s could still be managed. It should be noted that even if acceptable particle encapsulation may be achieved, different-sized droplets are not useful in most applications.

Increasing Ca to Ca = 0.03 resulted in having a range of droplets with $90 \leq d \leq 153\,\mu$m, making it almost impossible to synchronize the particle and droplet frequencies because each specific size of droplet needs a certain amount of time to detach and form. Droplet generation frequency is much higher than other cases ($f > 500$ Hz), not allowing full control of encapsulation by monitoring s. Figure 12(b) demonstrates that for Ca = 0.03, at $s = 100\,\mu$m, the maximum relative frequency for 1 particle/drop equal to 65% is achieved. This deficiency is much below what we achieved in squeezing and dripping. As jetting is not a favorable regime to work with and controlling the system's behavior is difficult, we do not go into further details about this regime.

D. Expected number of particles per droplet

The expected number of particles encapsulated per droplet (ENPD) as a function of relevant parameters is plotted in Fig. 13 by interpolating our findings (black circles), in which the red, white, and blue colors represent having exactly 2, 1, and 0 particles in droplets. The white area is the recommended zone to maximize encapsulation efficiency. Figure 13(a) shows the effect of Ca on ENPD in a range of s; it can be used to choose optimum s for different Ca. As changing Ca causes changes in d, Fig. 13(b) helps to choose s for the desirable droplet size. For instance, at Ca = 0.01, any $s < 300\,\mu$m, would fall under the red zone indicating that most droplets have two particles. Increasing s until reaching the white zone enhances the chance of single encapsulation, that is, ENPD = 1. Any set of parameters that falls in the blue zone results in a larger number of empty droplets. d is negatively correlated with Ca, and that effect is manifested in Fig. 13 as well. When Ca increases, s needs to be reduced to provide enough particles for the droplets. In high Ca and small d, the blue zone is bigger than the other two, meaning that droplet generation is susceptible to generating empty droplets due to the fact that shear force is high, causing droplets to be generated rapidly without a chance to encapsulate a particle. On the other hand, for large values of s, the red zone expands. As the droplet size increases, the detachment takes longer, so 2 particles would have enough time to reach and pass the droplet generation junction and be trapped in droplets. Summing up, the dripping regime is the optimum choice for particle encapsulation as it not only has the potential to deliver full control over the encapsulation process, but also forms monodispersed droplets.

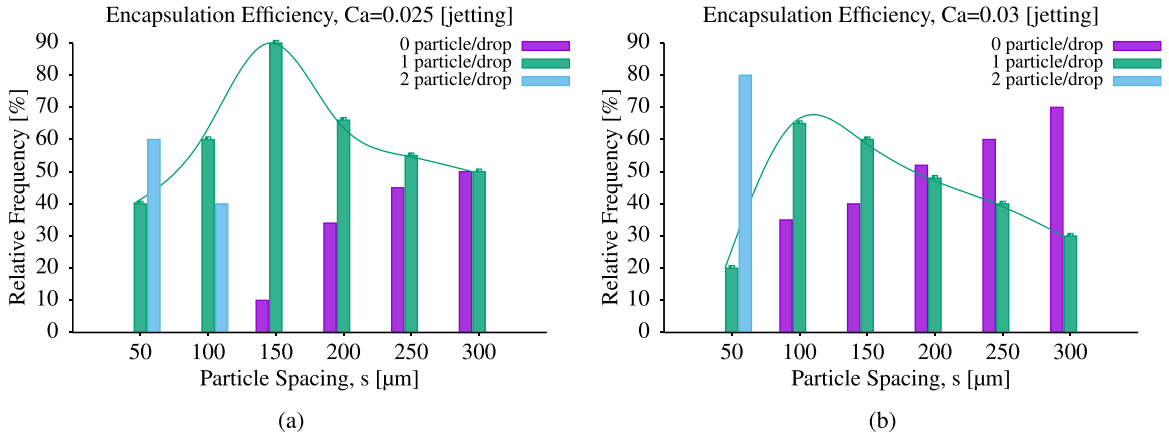

FIG. 12. Jetting: effect of particle spacing on particle encapsulation in jetting regime at (a) Ca = 0.025 and (b) Ca = 0.03.

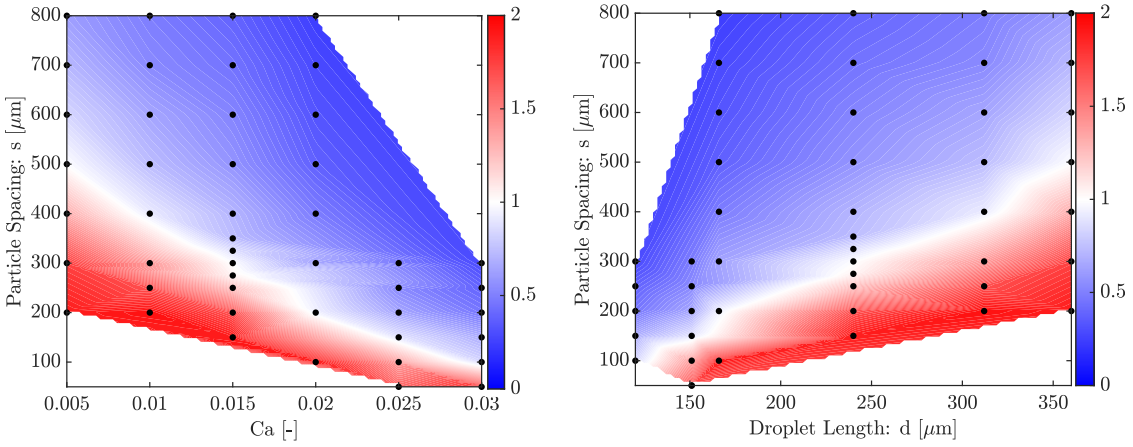

FIG. 13. ENPD in all the simulations done in this work. The effect of (a) Ca and (b) d on ENPD in a range of s is depicted. The black circles represent the location of test points; i.e., the simulations done, and the color bar shows ENPD. The white region indicates ENPD = 1.

V. CONCLUSIONS

The *MPPICInterFoam* solver in *OpenFOAM*-v2012 was used to simulate the encapsulation process of particles into liquid droplets generated by a high-throughput flow-focusing microfluidic device. The adopted method was validated against the experimental findings reported in Beneyton *et al.*,[16] showing a good agreement, especially in terms of the volume of the generated droplets.

We first provided insight into the physics involved in droplet generation and particle encapsulation. Specifically, we investigated how velocity profiles, streamlines, and circulation areas affect particle movements. Single particle or cell encapsulation in droplet microfluidics is a well-known problem due to random particle encapsulation. We focused on improving the single encapsulation efficiency in droplet microfluidics by analyzing the effect of particle pre-ordering on particle encapsulation in different droplet generation regimes. These are obtained by varying the capillary number. Our results show that each formed droplet would encapsulate exactly one solid particle only for a specific combination of Ca and s in the squeezing—Ca = 0.005, 0.01 and s = 500, 400 μm, respectively—and dripping—Ca = 0.015, 0.02 and s = 300, 200 μm, respectively—regimes. Scenarios characterized by smaller values of the particle spacing result in two particles per droplet. Conversely, larger values of s lead to many empty droplets. In the squeezing regime, although one can obtain the encapsulation of exactly one particle in monodispersed droplets, a low speed of droplet generation may act as a hurdle. Dripping with bigger Ca offers a higher number of monodispersed droplets with one particle entrapped. In the dripping regime, a smaller s compared to squeezing gives an efficiency of $\sim$ 100%. Yet, in this regime, a slight change in s may have a large impact on encapsulation results. Thus, more precautions in the ordering of particles before reaching the cross-junction are required. When considering jetting, even though much higher droplet frequencies can be achieved, the droplets are polydispersed and have different sizes. This makes it difficult to synchronize the droplet and particle frequencies to gain full control over encapsulation. We can conclude that the dripping regime is the most favorable one. For this regime, we investigated the susceptibility to a variation of the junction angle θ and found that $\theta = 60^\circ$ optimizes monodispersity and encapsulation efficiency.

Our proposed future work includes testing different and more complicated arrangements of particles at the inlet, adapting the immersed boundary method[48] to simulate the presence of larger particles in the microfluidic channel; comparing the adopted solver against findings obtained by different implementations of the lattice Boltzmann method;[49,50] and checking if the boundaries of solver can be pushed further.

ACKNOWLEDGMENTS

We would like to thank Dr. Philip Day for his valuable consults. This research was funded by the Department of Mechanical, Aerospace and Civil Engineering, the University of Manchester, under the Exceptional Women in Engineering Ph.D. scholarship scheme.

AUTHOR DECLARATIONS

Conflict of Interest

The authors have no conflicts to disclose.

Author Contributions

Maryam Fatehifar: Conceptualization (equal); Data curation (lead); Formal analysis (lead); Investigation (lead); Methodology (lead); Software (lead); Validation (lead); Visualization (lead); Writing – original draft (lead); Writing – review & editing (equal). **Alistair James Revell:** Conceptualization (equal); Investigation (supporting); Software (supporting); Supervision (lead); Writing – review & editing (equal). **Masoud Jabbari:** Conceptualization (supporting); Supervision (supporting); Writing – review & editing (equal). **Alessandro De Rosis:** Investigation (supporting); Supervision (supporting); Writing – review & editing (equal).

DATA AVAILABILITY

The data that support the findings of this study are available from the corresponding author upon reasonable request.

REFERENCES

[1]N. Paiboon, S. Surassmo, U. R. Ruktanonchai, and A. Soottitantawat, "Hydrodynamic control of droplet formation in narrowing jet and tip streaming regime using microfluidic flow-focusing," Int. J. Multiphase Flow **150**, 104013 (2022).

[2]K.-H. Chen, C.-C. Liu, S.-Y. Lu, S.-J. Chen, F. Sheu, and L.-M. Fu, "Rapid microfluidic analysis detection system for sodium dehydroacetate in foods," Chem. Eng. J. **427**, 131530 (2022).

[3]S. S. S. Zadeh, V. Egan, and P. Walsh, "An experimental study on the mobility of droplets in liquid-liquid Taylor flows within circular capillaries," Int. J. Multiphase Flow **157**, 104259 (2022).

[4]L. Amirifar, M. Besanjideh, R. Nasiri, A. Shamloo, F. Nasrollahi, N. R. de Barros, E. Davoodi, A. Erdem, M. Mahmoodi, V. Hosseini *et al.*, "Droplet-based microfluidics in biomedical applications," Biofabrication **14**, 022001 (2022).

[5]S. Naji, A. Rahimi, V. Bazargan, and M. Marengo, "Numerical and artificial neural network analysis of an axisymmetric co-flow-focusing microfluidic droplet generator using active and passive control," Phys. Fluids **35**, 062008 (2023).

[6]P. Zhu and L. Wang, "Passive and active droplet generation with microfluidics: A review," Lab Chip **17**, 34–75 (2017).

[7]S. J. Hymel, H. Lan, H. Fujioka, and D. B. Khismatullin, "Cell trapping in Y-junction microchannels: A numerical study of the bifurcation angle effect in inertial microfluidics," Phys. Fluids **31**, 082003 (2019).

[8]U. Banerjee, S. Jain, and A. Sen, "Particle encapsulation in aqueous ferrofluid drops and sorting of particle-encapsulating drops from empty drops using a magnetic field," Soft Matter **17**, 6020–6028 (2021).

[9]S. G. Sontti and A. Atta, "Regulation of droplet size and flow regime by geometrical confinement in a microfluidic flow-focusing device," Phys. Fluids **35**, 012010 (2023).

[10]X. Li, L. He, Y. He, H. Gu, and M. Liu, "Numerical study of droplet formation in the ordinary and modified T-junctions," Phys. Fluids **31**, 082101 (2019).

[11]M. H. Javanmard, F. Niksirat, and M. K. Moraveji, "Effects of topological changes in microchannel geometries on the hydrodynamic formation and breakup of all-aqueous droplets," Phys. Fluids **34**, 052009 (2022).

[12]D. J. Collins, A. Neild, A. DeMello, A.-Q. Liu, and Y. Ai, "The Poisson distribution and beyond: Methods for microfluidic droplet production and single cell encapsulation," Lab Chip **15**, 3439–3459 (2015).

[13]Y. Zhang and H.-R. Jiang, "A review on continuous-flow microfluidic PCR in droplets: Advances, challenges and future," Anal. Chim. Acta **914**, 7–16 (2016).

[14]M. Fatehifar, A. Revell, and M. Jabbari, "Non-Newtonian droplet generation in a cross-junction microfluidic channel," Polymers **13**, 1915 (2021).

[15]S. G. Sontti and A. Atta, "CFD analysis of microfluidic droplet formation in non-Newtonian liquid," Chem. Eng. J. **330**, 245–261 (2017).

[16]T. Beneyton, I. Wijaya, P. Postros, M. Najah, P. Leblond, A. Couvent, E. Mayot, A. D. Griffiths, and A. Drevelle, "High-throughput screening of filamentous fungi using nanoliter-range droplet-based microfluidics," Sci. Rep. **6**, 27223 (2016).

[17]S. K. Jena, T. Srivastava, S. S. Bahga, and S. Kondaraju, "Effect of channel width on droplet generation inside T-junction microchannel," Phys. Fluids **35**, 022107 (2023).

[18]P. Giefer, A. Kyrloglou, and U. Fritsching, "Impact of wettability on interface deformation and droplet breakup in microcapillaries," Phys. Fluids **35**, 042110 (2023).

[19]J. F. Edd, D. Di Carlo, K. J. Humphry, S. Köster, D. Irimia, D. A. Weitz, and M. Toner, "Controlled encapsulation of single-cells into monodisperse picolitre drops," Lab Chip **8**, 1262–1264 (2008).

[20]K. Shahrivar and F. Del Giudice, "Controlled viscoelastic particle encapsulation in microfluidic devices," Soft Matter **17**, 8068–8077 (2021).

[21]S. Kahkeshani, H. Haddadi, and D. Di Carlo, "Preferred interparticle spacings in trains of particles in inertial microchannel flows," J. Fluid Mech. **786**, R3 (2016).

[22]M. K. Alam, E. Koomson, H. Zou, C. Yi, C.-W. Li, T. Xu, and M. Yang, "Recent advances in microfluidic technology for manipulation and analysis of biological cells (2007–2017)," Anal. Chim. Acta **1044**, 29–65 (2018).

[23]A. Shamloo and F. Y. Parast, "Simulation of blood particle separation in a trapezoidal microfluidic device by acoustic force," IEEE Trans. Electron Devices **66**, 1495–1503 (2019).

[24]K. Shahrivar and F. Del Giudice, "Beating Poisson stochastic particle encapsulation in flow-focusing microfluidic devices using viscoelastic liquids," Soft Matter **18**, 5928 (2022).

[25]J. Yu, W. Huang, L. Chin, L. Lei, Z. Lin, W. Ser, H. Chen, T. Ayi, P. Yap, C. Chen *et al.*, "Droplet optofluidic imaging for λ-bacteriophage detection *via* co-culture with host cell *Escherichia coli*," Lab Chip **14**, 3519–3524 (2014).

[26]B. L. Wang, A. Ghaderi, H. Zhou, J. Agresti, D. A. Weitz, G. R. Fink, and G. Stephanopoulos, "Microfluidic high-throughput culturing of single cells for selection based on extracellular metabolite production or consumption," Nat. Biotechnol. **32**, 473–478 (2014).

[27]M. Heinrich and R. Schwarze, "3D-coupling of volume-of-fluid and Lagrangian particle tracking for spray atomization simulation in OpenFOAM," SoftwareX **11**, 100483 (2020).

[28]H. Yang, "Numerical study on droplet formation and cell encapsulation process in a micro T-junction via lattice Boltzmann method," Ph.D. thesis (The Ohio State University, 2013).

[29]M. Yaghoobi, M. S. Saidi, S. Ghadami, and N. Kashaninejad, "An interface–particle interaction approach for evaluation of the co-encapsulation efficiency of cells in a flow-focusing droplet generator," Sensors **20**, 3774–3790 (2020).

[30]M. Outokesh, H. A. Amiri, and M. Miansari, "Numerical insights into magnetic particle enrichment and separation in an integrated droplet microfluidic system," Chem. Eng. Process.: Process Intensif. **170**, 108696–108709 (2022).

[31]M. J. Andrews and P. J. O'Rourke, "The multiphase particle-in-cell (MP-PIC) method for dense particulate flows," Int. J. Multiphase Flow **22**, 379–402 (1996).

[32]S. H. Kim, J. H. Lee, and R. D. Braatz, "Multi-phase particle-in-cell coupled with population balance equation (MP-PIC-PBE) method for multiscale computational fluid dynamics simulation," Comput. Chem. Eng. **134**, 106686 (2020).

[33]M. Kumar, R. Reddy, R. Banerjee, and N. Mangadoddy, "Effect of particle concentration on turbulent modulation inside hydrocyclone using coupled MPPIC-VOF method," Sep. Purif. Technol. **266**, 118206 (2021).

[34]U. Caliskan and S. Miskovic, "A chimera approach for MP-PIC simulations of dense particulate flows using large parcel size relative to the computational cell size," Chem. Eng. J. Adv. **5**, 100054 (2021).

[35]C. Y. Wen and Y. H. Yu, "Mechanics of fluidization," in *Fluid Particle Technology*, Chemical Engineering Progress Symposium Series (American Institute of Chemical Engineers, 1966), Vol. 62, pp. 100–111.

[36]D. Stoecklein and D. Di Carlo, "Nonlinear microfluidics," Anal. Chem. **91**, 296–314 (2019).

[37]J.-Y. Kwon, T. Kim, J. Kim, and Y. Cho, "Particle focusing under Newtonian and viscoelastic flow in a straight rhombic microchannel," Micromachines **11**, 998 (2020).

[38]C. Prohm and H. Stark, "Feedback control of inertial microfluidics using axial control forces," Lab Chip **14**, 2115–2123 (2014).

[39]D. Di Carlo, D. Irimia, R. G. Tompkins, and M. Toner, "Continuous inertial focusing, ordering, and separation of particles in microchannels," Proc. Natl. Acad. Sci. **104**, 18892–18897 (2007).

[40]G. Y. Soh, G. H. Yeoh, and V. Timchenko, "Numerical investigation on the velocity fields during droplet formation in a microfluidic T-junction," Chem. Eng. Sci. **139**, 99–108 (2016).

[41]M. Nooranidoost and R. Kumar, "Improving viability of leukemia cells by tailoring shell fluid rheology in constricted microcapillary," Sci. Rep. **10**, 11570 (2020).

[42]M. Kalli, P. Pico, L. Chagot, L. Kahouadji, S. Shin, J. Chergui, D. Juric, O. Matar, and P. Angeli, "Effect of surfactants during drop formation in a microfluidic channel: A combined experimental and computational fluid dynamics approach," J. Fluid Mech. **961**, A15 (2023).

[43]M. Sesen, T. Alan, and A. Neild, "Droplet control technologies for microfluidic high throughput screening (μHTS)," Lab Chip **17**, 2372–2394 (2017).
[44]L. Sheng, L. Ma, Y. Chen, J. Deng, and G. Luo, "A comprehensive study of droplet formation in a capillary embedded step T-junction: From squeezing to jetting," Chem. Eng. J. **427**, 132067 (2022).
[45]S. G. Sontti and A. Atta, "Numerical insights on controlled droplet formation in a microfluidic flow-focusing device," Ind. Eng. Chem. Res. **59**, 3702–3716 (2020).
[46]C. Zhou, P. Yue, and J. J. Feng, "Formation of simple and compound drops in microfluidic devices," Phys. Fluids **18**, 092105 (2006).
[47]T. Fu, Y. Wu, Y. Ma, and H. Z. Li, "Droplet formation and breakup dynamics in microfluidic flow-focusing devices: From dripping to jetting," Chem. Eng. Sci. **84**, 207–217 (2012).
[48]C. S. Peskin, "The immersed boundary method," Acta Numer. **11**, 479–517 (2002).
[49]G. Wang, L. Fei, and K. H. Luo, "Lattice Boltzmann simulation of a water droplet penetrating a micropillar array in a microchannel," Phys. Fluids **33**, 043308 (2021).
[50]A. De Rosis and E. Enan, "A three-dimensional phase-field lattice Boltzmann method for incompressible two-components flows," Phys. Fluids **33**, 043315 (2021).